Energy Advances

ROYAL SOCIETY OF CHEMISTRY

PAPER

View Article Online
View Journal | View Issue

Cite this: *Energy Adv.*, 2026, 5, 315

Synergistic interactions in $LaMnO_3$/CuO composites with enhanced supercapacitive performance

Alisha Dhakal, *[a] Felio R. Perez,[b] Shawn David Pollard[a] and Sanjay R. Mishra*[a]

Received 21st November 2025,
Accepted 4th February 2026

DOI: 10.1039/d5ya00339c

rsc.li/energy-advances

Composites of La-based perovskites with metal oxides have attracted significant attention in electrochemistry owing to their synergistic effects. In this work, $LaMnO_3$ (LMO)/CuO composites with varying ratios of (100–*x*)% LMO : *x*% CuO (where wt% *x* = 0, 10, 30, 50, and 100) were successfully synthesized *via* autocombustion technique followed by annealing at 1000 °C. The morphology and phase purity of the composites were confirmed by X-ray diffraction (XRD) and field-emission scanning electron microscopy (FESEM), respectively. Among all compositions, LMO/CuO(9 : 1) exhibited the highest BET specific surface area of 14 $m^2\ g^{-1}$ with an average pore size of 2.11 nm. Compared to single-phase $LaMnO_3$ or CuO, the composites demonstrated increased oxygen vacancies, as confirmed by XPS O 1s spectra. These structural features directly contributed to superior electrochemical performance, with LMO/CuO(9 : 1) achieving a specific capacitance (C_{SP}) of 646.8 F g^{-1} at 1 mV s^{-1} and 517.1 F g^{-1} at 1 A g^{-1}. Furthermore, it delivered an energy density (E_d) of 25.8 Wh kg^{-1} at a power density (P_d) of 397.6 W kg^{-1}, along with excellent cyclic stability, retaining 99.8% capacitance after 5000 charge/discharge cycles. These findings underscore the crucial role of synergistic interactions between $LaMnO_3$ and CuO in enhancing electrochemical performance, thereby positioning LMO/CuO composites as promising candidates for next-generation energy storage materials.

Introduction

The global population is increasing, while fossil fuel resources are depleting rapidly. To address the energy crisis, there is an increasing demand for sustainable energy storage/conversion devices that must possess high energy density (E_d)/power density (P_d), long cyclic stability, and be environmentally friendly.[1–4] Supercapacitors represent one class of energy-storage devices capable of meeting these requirements and are generally categorized into three types: (i) electric double-layer capacitors (EDLCs), (ii) pseudocapacitors, and (iii) hybrid capacitors.[5] In EDLCs, charges are deposited on the surface without any chemical changes, making it a non-faradaic system. On the other hand, faradaic reactions, in which oxidation and reduction occur at the anode and cathode, are also involved and are referred to as pseudocapacitors.[6] A hybrid supercapacitor combines EDLCs and pseudocapacitors. Carbon-based materials operate *via* the EDLC mechanism to store energy, with higher charge/discharge rates, higher power density, and longer lifetimes.[7,8] However, carbon-based materials have a lower energy density than batteries.[9]

The charge-storage mechanism in transition-metal oxides, including Mn_2O_3, RuO_2, $NiCo_2O_4$, Co_3O_4, and V_2O_5, and mixed oxides such as perovskites, plays a critical role in pseudocapacitive energy-storage applications, owing to their ability to adopt multiple oxidation states and their stable morphology and high structural integrity.[10] They offer high specific capacitance (C_{SP})[6] due to fast, reversible redox reactions and higher E_d. Among oxides, RuO_2 exhibits a high $C_{SP} \sim 1580$ F g^{-1} at 1 mV s^{-1}.[11,12] However, the high cost makes RuO_2 less attractive for commercialization. Overcoming these limitations is crucial to meet the benchmark requirements for widespread commercial adoption.

Perovskite-type oxides have attracted considerable interest for supercapacitor applications due to their favorable physical and chemical properties, oxygen storage (inherent to oxygen vacancies), high electrical conductivity, thermal stability, and low cost.[13,14] The perovskites are in the form of ABO_3 (A is a lanthanide, B is a transition metal).[15] Among perovskite materials studied for supercapacitors, LaMnO3 has attracted considerable attention owing to its unique combination of La and Mn atoms. In the presence of oxygen vacancies, $LaMnO_3$

[a] *Department of Physics and Materials Science, The University of Memphis, Memphis, Tennessee 38152, USA. E-mail: srmishra@memphis.edu, adhakal@memphis.edu*
[b] *Integrated Microscopy Center, The University of Memphis, Memphis, Tennessee 38152, USA*

perovskites ($LaMnO_{3-\delta}$) lead to a partial reduction of Mn^{3+} ions to Mn^{2+} ions. These vacancies facilitate anionic intercalation, and Mn ions return to their original ionic states (Mn^{2+} and Mn^{3+}), thereby enhancing the material's supercapacitance,[16] Conversely, excess oxygen ($LaMnO_{3+\delta}$) promotes further oxidation of Mn^{3+} to Mn^{4+}.[12] However, its low specific surface area and tendency to agglomerate decrease its electrochemical performance. To overcome this problem, perovskites are often mixed with other metal oxides or carbon-based compounds. Among metal oxides, CuO is a promising candidate owing to its natural abundance, cost-effectiveness, eco-friendliness, ease of synthesis, and high theoretical capacitance (1783 F g^{-1}).[17]

For example, A. Arya *et al.* synthesized $LaMnO_3$–NiO composites *via* a sol–gel-assisted hydrothermal method and obtained a C_{SP} of 170 F g^{-1} at 10 mV s^{-1}. This improvement was attributed to the synergistic interaction between $LaMnO_3$ and NiO, which enhanced both ion transport efficiency and faradaic redox reactions.[18] A. Dhakal *et al.* followed the autocombustion method to synthesize $LaMnO_3$–Mn_3O_4 composites and reported a C_{SP} of 660 F g^{-1} at 1 A g^{-1} in 6 M KOH.[19] P. M. Shafi *et al.* synthesized $LaMnO_3$/rGO/PANI through a situ polymerization route with a C_{SP} of 802 F g^{-1} at 1 A g^{-1} in 3 M KOH.[20] The improved C_{SP} was attributed to the higher specific surface area and a greater number of electroactive sites. B. Patil *et al.* prepared $LaMnO_3$–rGO composites by mixing the components and performing electrochemical measurements in 1 M Na_2SO_4. The C_{SP} of $LaMnO_3$/rGO75% displayed a high value of 641 F g^{-1} at 1 A g^{-1} due to the larger surface area and high electrical conductivity of rGO and oxygen vacancy in $LaMnO_3$.[21] $LaMnO_3$–CeO_2 composites were synthesized *via* a hydrothermal method by S. Nagamuthu *et al.*, achieving a C_{SP} of 262 F g^{-1} at 1 A g^{-1} in 1 M Na_2SO_4.[22] The enhanced C_{SP} was due to the synergistic redox activity of Ce/Mn ions and improved conductivity. R. Packiaraj *et al.* synthesized mixed metal oxides composed of ZnO–NiO–CuO through the sol–gel method and reported a high C_{SP} of 1831 F g^{-1} at 1 A g^{-1} in 2 M KOH, which was higher than that of single or binary metal oxides.[23] This performance improvement was attributed to the synergistic interactions among metal oxides, in which nickel and copper enhanced active-site density and electrical conductivity, while zinc contributed to good chemical and thermal stability. MnO_2–CuO was prepared by K. M. Racik *et al.* using a hydrothermal method and obtained the C_{SP} of 279.12 F g^{-1} at 0.5 A g^{-1} in 1 KOH.[24] The higher capacitance compared to the individual oxides was attributed to the combined effects of MnO_2's structural stability and CuO's high electrical conductivity.

Building on the argument above, in this study, we synthesized LMO/CuO composites *via* a facile autocombustion technique and systematically investigated their electrochemical performance in an aqueous electrolyte. The incorporation of CuO into $LaMnO_3$ is expected to enhance charge storage through synergistic effects arising from both structural and interfacial contributions. Lattice mismatch and strain at the disordered interface between oxide particles promote the formation of oxygen vacancies, thereby enabling polaron hopping.[25] The O^{2-}-deficient interface leaves behind localized electrons that stabilize mixed-valence states ($Mn^{3+}/Mn^{4+} \leftrightarrow Cu^{2+}/Cu^{+}$), broadening pseudocapacitive processes. The composite thus has a broader spectrum of accessible valence states with more charge storage per unit mass. Furthermore, the addition of secondary oxides prevents $LaMnO_3$ particles from agglomerating, thereby increasing the number of redox-active sites accessible to the electrolyte. Thus, the addition of CuO to $LaMnO_3$ forms heterojunctions that may reduce charge-transfer resistance, thereby enhancing electron mobility within the composite. Collectively, these effects could improve the C_{SP}, rate capability, and cyclic stability of the LMO/CuO composites.

Experimental

Synthesis of LMO composites

LMO/CuO composites were synthesized *via* an autocombustion method. In the first step, a 1 : 1 molar mixture of lanthanum(III) nitrate hexahydrate and manganese(II) nitrate tetrahydrate, with a 1 : 1 metal nitrate-to-citric acid monohydrate ratio, was dissolved in 30 mL of deionized (DI) water to prepare solution 1. Similarly, copper(II) nitrate hemipentahydrate and citric acid monohydrate were dissolved in 30 mL of DI water to form solution 2. Both solutions were magnetically stirred separately for 30 min. Solution 2 was added to solution 1 under continuous magnetic stirring until a homogeneous mixture was obtained. After 15 minutes, the mixture was heated to 120 °C until auto-ignition occurred. The resulting powder was transferred to a furnace and annealed at 1000 °C for 16 hours. The final product was obtained as LMO/CuO(100–x)%: x%, (with Wt% x = 0, 100, 10, 30, and 50) composites named as LMO/CuO(1 : 0), LMO/CuO(0 : 1), LMO/CuO(9 : 1), LMO/CuO(7 : 3), and LMO/CuO(1 : 1), respectively. The chemical reaction for the formation of LMO/CuO composites is presented in Scheme 1 and eqn (1).

$$La(NO_3)_3{\cdot}6H_2O + Mn(NO_3)_2{\cdot}4H_2O + Cu(NO_3)_2{\cdot}2.5H_2O + C_6H_8O_7{\cdot}H_2O \rightarrow LaMnO_3 + CuO + 7/2\ N_2 + 6CO_2 + 27/2\ H_2O + 6O_2 \quad (1)$$

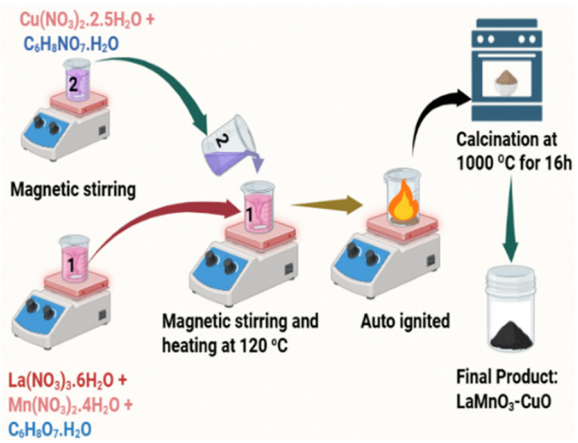

Scheme 1 Schematic diagram of the synthesis of LMO/CuO composites *via* the autocombustion technique.

Preparation of the electrode

To clean the substrate (Ni-foam) and the electrode, the preparation method described in our previous work is followed.[26] Briefly, the Ni-foam was cleaned by sequential ultrasonication for 10 minutes each in 16 mL of 37 wt% HCl, deionized (DI) water, and ethanol, followed by drying at 110 °C for 2 hours. For electrode fabrication, an electrode solution was prepared by dispersing 6 mg of LMO/CuO composite and 1 mg of polyvinylidene fluoride (PVDF) in 1 mL of *N*-methyl-2-pyrrolidone (NMP) under magnetic stirring. A volume of 0.6 mL of this homogeneous mixture was uniformly coated onto the pre-cleaned Ni-foam and then dried at 100 °C for 20 hours in a vacuum furnace. The active material loading was determined by subtracting the bare Ni-foam's original mass from that of the coated, dried electrode.

Characterization

The prepared LMO/CuO composites were characterized using various analytical tools. The crystal structure and phase studies were conducted using XRD (Bruker D8 with Cu Kα1 radiation) and FESEM (Hitachi S-470). The elemental and chemical compositions were investigated using energy-dispersive X-ray spectroscopy (EDX; Bruker Esprit Spectrum 2.3) and X-ray photoelectron spectroscopy (XPS; Thermo Scientific K-Alpha). The surface area and porosity of the composites were measured using a NOVAtouch surface area analyzer (Quantachrome Instruments).

Electrochemical analysis

Electrochemical measurements were performed in a three-electrode configuration in a 1 M KOH electrolyte at ambient temperature using a Gamry instrument (IFC1000-07045). The Ag/AgCl electrode served as the reference electrode, a platinum plate as the counter electrode, and LMO/CuO composites coated on nickel foam as the working electrode. Cyclic voltammetry (CV) was performed at scan rates from 1 to 200 mV s^{-1} over a potential window of 0 to 0.6 V. Chronopotentiometry (charge–discharge) tests were conducted at various current densities within a voltage range of 0 to 0.45 V. Electrochemical impedance spectroscopy (EIS) was recorded in the frequency range from 10 mHz to 100 kHz. The C_{SP}, (F g^{-1}), E_d (Wh kg^{-1}), and P_d (W kg^{-1}) were calculated from the CV and charge–discharge (GCD) data using eqn (2)–(5).[27–30]

$$C_{SP} = \frac{1}{mv(V_2 - V_1)}\int_{V_1}^{V_2} I(V)\mathrm{d}V \quad (2)$$

$$C_{SP} = \frac{I_m \times \Delta t}{\Delta V} \quad (3)$$

$$E_d = \frac{0.5 \times C_{SP} \times \Delta V^2}{3.6} \quad (4)$$

$$P_d = \frac{3600 \times E_d}{\Delta t} \quad (5)$$

where, $\int_{V_1}^{V_2} I(V)\mathrm{d}V$ gives the area enclosed in the CV curves, m implies mass of the active material in the electrode, v (mV s^{-1}) represents scan rate, V_2–V_1 (ΔV) is a potential window, $I(V)$ corresponds to the response current, I_m denotes the current density, and Δt denotes the discharge time.

Results and discussion

Structure and morphology

Fig. 1(a) presents the crystalline phases of LMO/CuO(1 : 0, 0 : 1, 9 : 1, 7 : 3, and 1 : 1) composites as determined by powder XRD at

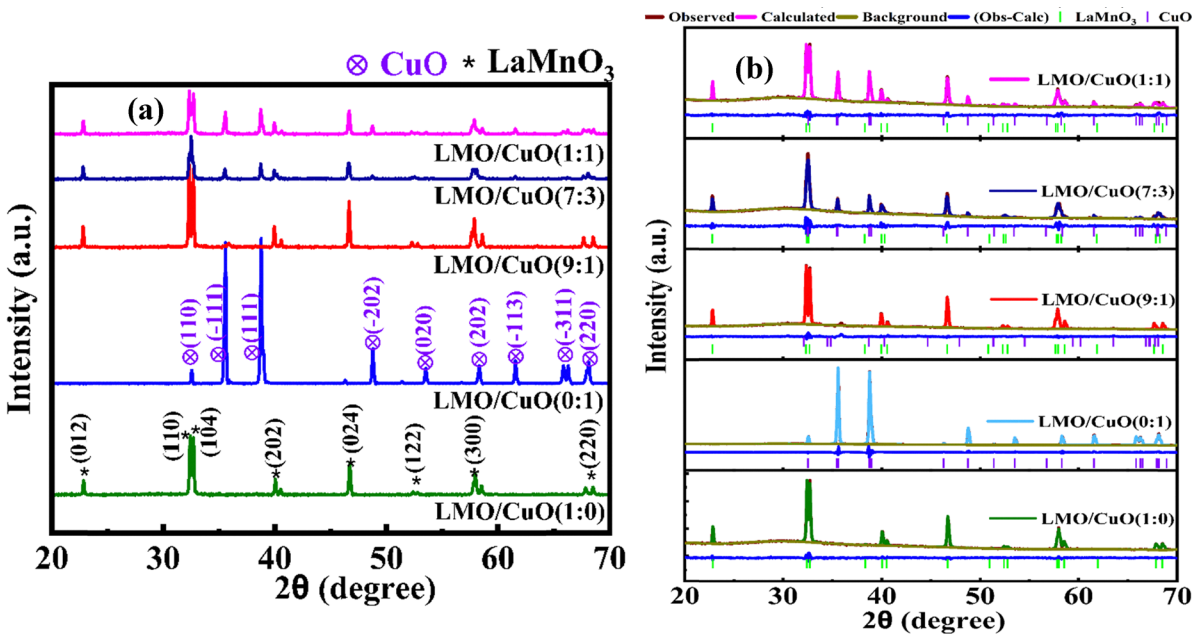

Fig. 1 (a) XRD pattern of LMO/CuO composites. (b) Rietveld refinement of XRD data for LMO/CuO composites was performed using GSAS-II.

room temperature. The composites LMO/CuO(1 : 0) only exhibit a single phase of $LaMnO_3$ with prominent diffraction peaks at 22.83, 32.34, 32.68, 39.95, 46.64, 52.31, 57.68, and 67.69°, corresponding to (012), (110), (104), (202), (024), (122), (300), and (220) crystal planes of $LaMnO_3$ with a rhombohedral crystal structure and space group of $R\bar{3}c$ (167) (PDF 01-076-9017). Similarly, for the molar ratio of LMO/CuO(0 : 1), the main diffraction peaks at 32.54, 35.59, 38.72, 48.76, 53.59, 58.19, 61.60, 66.24, and 68.17 correspond to the (110), ($\bar{1}$11), (111), ($\bar{2}$02), (020), (202), ($\bar{1}$13), ($\bar{3}$11), and (220), crystal planes of CuO with a monoclinic crystal structure and space group $C2/c$[15] (PDF 01-085-7183). However, the remaining three composites exhibit both distinguishable $LaMnO_3$ and CuO phases, with no other impurities present. Fig. 1(b) presents the Rietveld-refined XRD patterns of the LMO/CuO composites obtained using GSAS-II. The estimated composition of composites extracted from the Rietveld refinement are; LMO/CuO(100% : 0%), LMO/CuO(0% : 100%), LMO/CuO(84% : 16%), LMO/CuO(75% : 25%), and LMO/CuO(65% : 35%) for samples LMO/CuO(1 : 0), LMO/CuO(0 : 1), LMO/CuO(9 : 1), LMO/CuO(7 : 3), and LMO/CuO(1 : 1), respectively. The crystallite size was calculated using the Scherrer equation $D = \frac{K\lambda}{\beta \times \cos\theta}$,[31] where D is the crystallite size (nm), K is the Scherrer constant (0.9), λ is the X-ray wavelength (1.5406 Å), β is the full width at half maximum (FWHM) of the diffraction peak, and θ is the Bragg diffraction angle. The characteristic diffraction peaks (2θ) of $LaMnO_3$ were observed at 22.83, 32.34, 32.68, 39.95, and 46.64°, while those of CuO appeared at 35.59, 38.72, 48.76, and 61.60°. The calculated crystallite sizes of $LaMnO_3$ and CuO are summarized in Table S1.

The FESEM images in Fig. 2(a–e) show the surface morphology of pure LMO/CuO composites with varying ratios (1 : 0, 0 : 1, 9 : 1, 7 : 3, and 1 : 1)). Fig. 2(a) shows the LMO/CuO(1 : 0) composites, which are spongier and more fragile with a chain-like structure. LMO/CuO(0 : 1) sample (Fig. 2(b)) displays a relatively dense and well-faceted crystalline structure, composed of tightly packed grains with smooth surfaces. The LMO/CuO composites exhibit distinct morphological transformations with varying CuO content. The LMO/CuO(9 : 1) sample (Fig. 2(c)) shows a porous and loosely aggregated structure, likely due to the dominant $LaMnO_3$ phase. As the CuO content increases in $LaMnO_3$ at a 7 : 3 ratio (Fig. 2(d)), the morphology resembles granular particles connected in a chain, with the presence of voids and open channels, indicating loosely packed particles and enhanced interparticle connectivity. At a 1 : 1 ratio (Fig. 2(e)), the microstructure appears highly uniform, with fine particles distributed densely across the surface between $LaMnO_3$ and CuO phases. The elementary mapping of O (red), La (blue), Mn (green), and Cu (magenta) is shown in Fig. S1. The corresponding EDX spectra (Fig. 2(a′–e′)) confirm the expected elemental composition of each sample. These EDX results validate the presence of La, Mn, Cu, and O in LMO/CuO composites.[32] Minor peaks for Au and C are also present, which are attributed to the gold coating and carbon tape used during FESEM sample preparation.

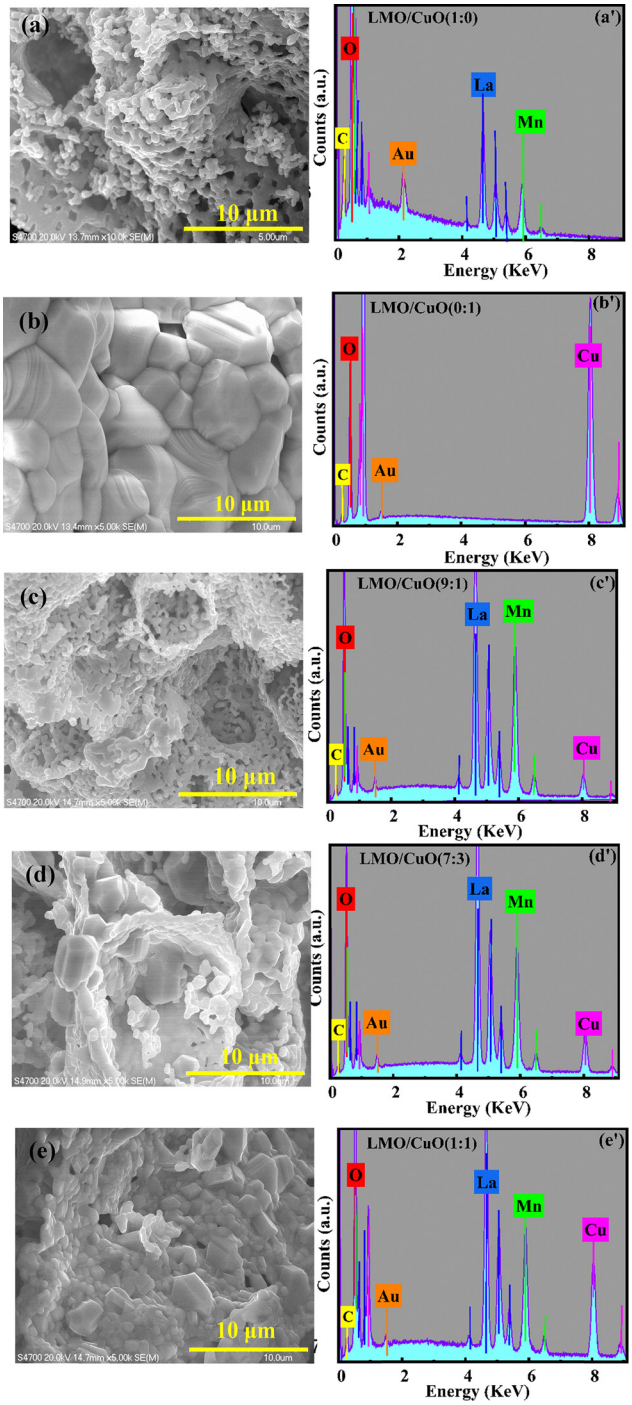

Fig. 2 (a–e) FESEM images and (a′–e′) elemental mapping of the LMO/CuO(1 : 0), LMO/CuO(0 : 1), LMO/CuO(9 : 1), LMO/CuO(7 : 3), and LMO/CuO(1 : 1) composites, respectively.

The surface area and pore size distribution of the LMO/CuO composites were evaluated using N_2 adsorption–desorption isotherms, as shown in Fig. 3(a–e). All curves show a gradual increase at low P/P_0, followed by a sharp rise near $P/P_0 \sim 0.9$–1.0, characteristic of type IV isotherms (IUPAC classification), typical of mesoporous materials. LMO/CuO(1 : 0), with a moderate slope and a rapid rise at high P/P_0, exhibits mesoporous

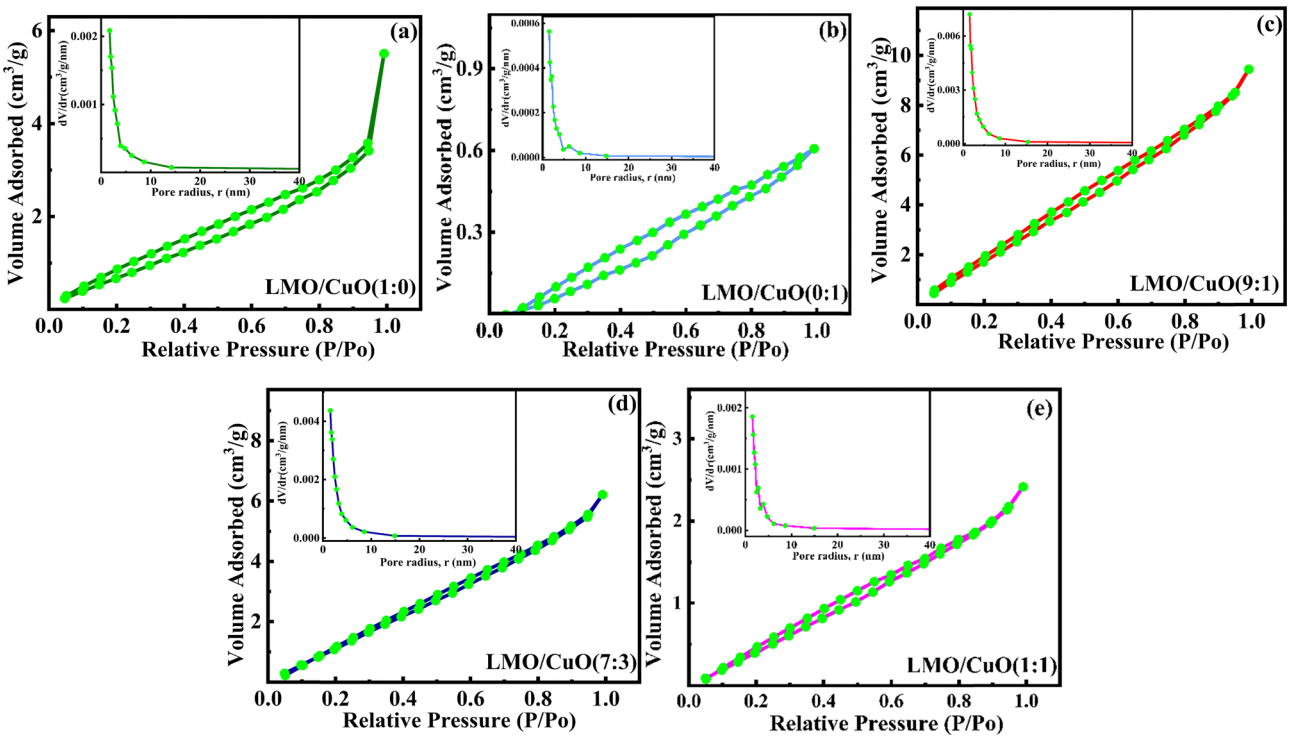

Fig. 3 N_2 adsorption–desorption isotherms of LMO/CuO composites (a–e) with corresponding BJH pore size distribution curves (insets).

behavior with a moderate surface area, whereas LMO/CuO(0 : 1), with much lower adsorption volume, may be due to a low surface area and few pores in CuO. Among the samples, LMO/CuO(9 : 1) exhibited the highest Brunauer–Emmett–Teller (BET) surface area of 13.82 $m^2\ g^{-1}$, while the BET values for all composites are summarized in Table S1. The pore volume and pore radius distribution, derived from Barrett–Joyner–Halenda (BJH) analysis of the desorption branch, are displayed in the inset Fig. 3(a–e), confirming the mesoporous nature of the composites. In all insets, the peak is sharply located below ~10 nm, averaging 2–5 nm, proving that the pores are mesoporous. Beyond 15 nm, d*V*/d*r* nearly drops to zero, indicating the absence of macropores in the compounds. Well-ordered porosity, as evidenced by a narrow pore-size distribution, could enhance ion diffusion in the electrode material.[33] Such mesoporosity, combined with a high specific surface area, facilitates efficient ion diffusion and charge transport, which are critical for enhanced electrochemical performance. Notably, CuO shows a very low specific surface area (Fig. 2(b)).

The chemical composition of LMO/CuO composites was determined by XPS analysis and presented in Fig. 4(a–e). Fig. 4(a) shows the La 3d XPS spectra, which exhibit distinct spin–orbit peaks at 834.4 and 838.0 eV, corresponding to La $3d_{5/2}$, along with additional peaks at 850.8 and 855.4 eV associated with La $3d_{3/2}$. These findings confirm the presence of La^{3+} in the LMO/CuO composites, which aligns with the results reported by.[22,34] Meanwhile, Fig. 4(b) presents the Mn 2p spectra, which reveal broad line widths and complex peak structures, indicating the coexistence of multiple Mn oxidation states. The major peaks observed at 639.98 eV and 651.78 eV correspond to Mn $2p_{3/2}$ and Mn $2p_{1/2}$, respectively,[35] with a consistent spin–orbit separation of approximately 11.8 eV. Each peak is further resolved into components attributed to Mn^{2+}, Mn^{3+}, and Mn^{4+} oxidation states (Fig. 4(d)). Specifically, peaks at 641.2 eV and 652.3 eV correspond to Mn^{2+}, those at 642.3 eV and 653.9 eV represent Mn^{3+}, and peaks at 644.0 eV and 655.5 eV relate to Mn^{4+}.[5,36,37]

Similarly, the deconvoluted Cu 2p XPS spectrum (Fig. 4(c)) reveals characteristic Cu^{2+} peaks at around 935.41 and 954.89 eV, along with Cu^{+} peaks located at 933.81 and 953.34 eV, respectively. In addition, two distinct satellite peaks are observed at 941.18 and 943.77 eV, further confirming the presence of multiple copper oxidation states.[38] The O 1s XPS spectra of transition metal oxides are deconvoluted into three Gaussian peaks, generally appearing in the ranges of 529–530 eV, 531–532 eV, and 532–535 eV, corresponding to lattice oxygen (O_1), oxygen vacancies (O_2), and chemisorbed oxygen species associated with surface hydroxyl groups (O_3), respectively.[39–41] As illustrated in Fig. 4(e), all three oxygen species O_1, O_2, and O_3 are observed in the spectra of single-phase $LaMnO_3$, CuO, and the LMO/CuO composites. The corresponding O_2/O_1 ratios are 0.66, 0.46, 0.95, 0.66, and 0.74 for LMO/CuO with ratios 1 : 0, 0 : 1, 9 : 1, 7 : 3, and 1 : 1, respectively. The nearly 1 : 1 O_2/O_1 ratio in LMO/CuO(9 : 1) composites indicates the presence of oxygen vacancies, providing further evidence of lattice-defect formation. The calculated Mn^{3+}/Mn^{2+} ratios were 1.68, 1.29, 1.31, and 1.33, while the Mn^{3+}/Mn^{4+} ratios were 1.69, 1.42, 1.36, and 1.23 for LMO/CuO(1 : 0), LMO/CuO(9 : 1), LMO/CuO(7 : 3), and LMO/CuO(1 : 1), respectively. Similarly, the Cu^{2+}/Cu^{1+} ratios were determined to be 2.12, 1.11, 0.86, and

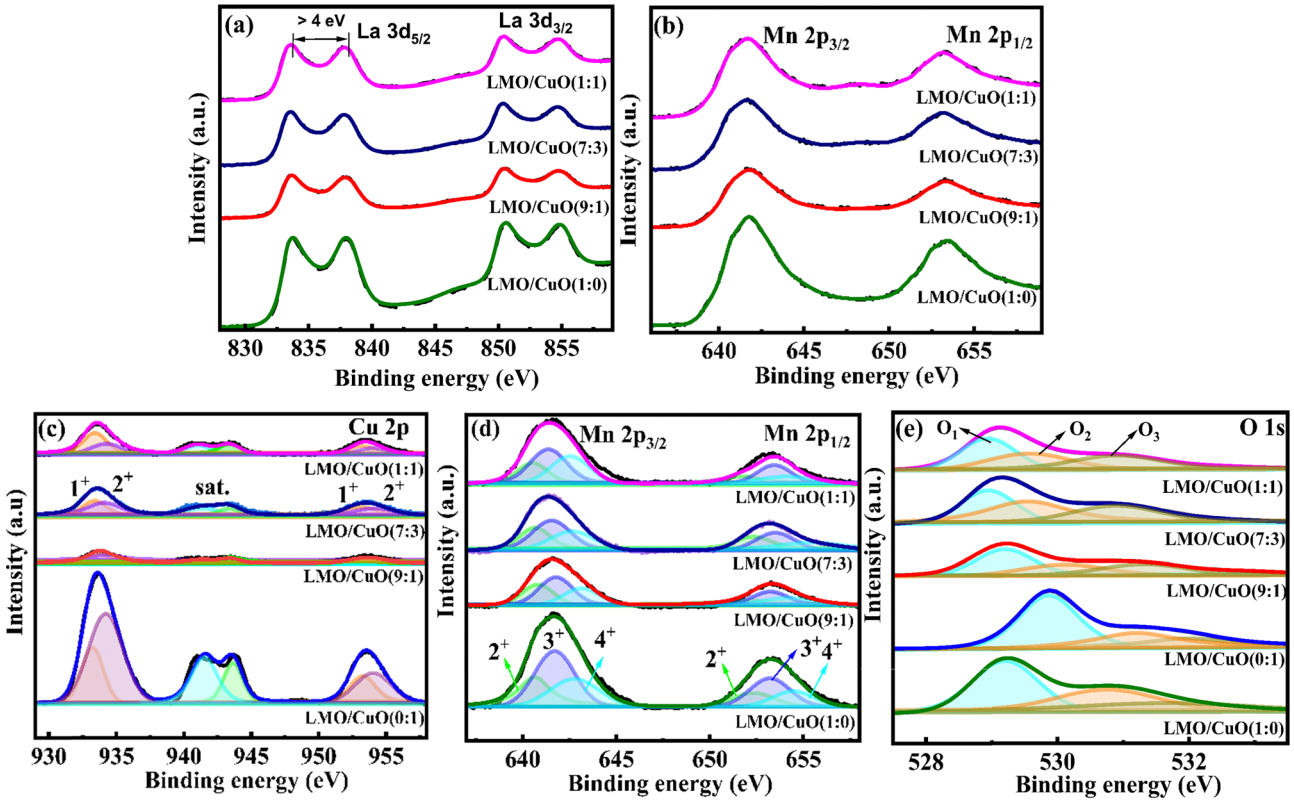

Fig. 4 XPS spectra of high-resolution of (a) La 3d and (b) Mn 2p and deconvoluted spectra of (c) Cu 2p, (d) Mn 2p, and (e) O 1s of LMO/CuO composites.

0.50 for LMO/CuO(0 : 1), LMO/CuO(9 : 1), LMO/CuO(7 : 3), and LMO/CuO(1 : 1), respectively. Notably, the LMO/CuO(9 : 1) composite exhibits a high Mn^{3+}/Mn^{4+} and Cu^{2+}/Cu^{1+} ratios, indicating that these oxidation states (Cu^{2+}, Mn^{3+}) can readily undergo reversible redox transitions, which is highly favorable for enhancing electrochemical activity.

Electrochemical analysis

Fig. 5(a) shows the CV curves of LMO/CuO composites at 1 mV s^{-1} in the potential range 0 to 0.6 V. Among them, LMO/CuO(9 : 1) CV curves enclosed the largest integral area, which indicates having a higher C_{SP}. Furthermore, Fig. 5(b) displays the chronopotentiometry charge/discharge curves of the LMO/CuO composite electrode at 1 A g^{-1}. The discharge time of the LMO/CuO(9 : 1) has the largest value compared to other composites, further highlighting its better performance in electrochemical properties. Based on XPS data and faradaic reaction, the possible oxygen intercalation/deintercalation reactions during the energy storage of $LaMnO_3$ and CuO are,[42–44]

$$La[Mn^{2+}_{2\delta},Mn^{3+}_{1-2\delta}]O_{3-\delta} + 2\delta OH^- \leftrightarrow LaMn^{3+}O_3 + \delta H_2O + 2\delta e^- \quad (6)$$

$$LaMn^{3+}O_3 + 2\delta OH^- \leftrightarrow La[Mn^{4+}_{2\delta},Mn^{3+}_{1-2\delta}]O_{3+\delta} + \delta H_2O + 2\delta e^- \quad (7)$$

$$2CuO + H_2O + 2e^- \leftrightarrow Cu_2O + 2OH^- \quad (8)$$

$$Cu_2O + H_2O + 2OH^- \leftrightarrow 2Cu(OH)_2 + 2e^- \quad (9)$$

The CV curves of the LMO/CuO composite electrode exhibit distinct pairs of redox peaks, indicative of strong faradaic behavior (Fig. 5(c)). Although the redox activity indicates effective charge-transfer processes, the individual peaks corresponding to $LaMnO_3$ and CuO are not clearly distinguishable due to their overlapping potential regions. As the scan rate increases from 1 to 200 mV s^{-1}, the anodic peaks shift to more positive potentials, while the cathodic peaks shift to more negative potentials. This behavior is attributed to enhanced electrical polarization and partially irreversible redox processes, suggesting that redox reactions occur more rapidly at the interface between the active electrode material and the electrolyte at higher scan rates.

Electrochemical energy storage processes can be classified as capacitive-controlled (capacitor-like) or diffusion-controlled (battery-like). To distinguish these kinetic contributions and understand the charge-storage behavior of electrode materials, electrochemical techniques such as cyclic voltammetry (CV) and electrochemical impedance spectroscopy (EIS) are commonly employed. In CV, the current response (i) as a function of the scan rate (ν) provides valuable insight into the underlying charge storage mechanism. This relationship is typically described by a power-law eqn (10):[45]

$$i = a\nu^b \quad (10)$$

where a is a constant and b is an exponent that indicates the dominant charge storage process. The b-value can be obtained from the slope of the log–log plot of peak current (i) *versus* scan

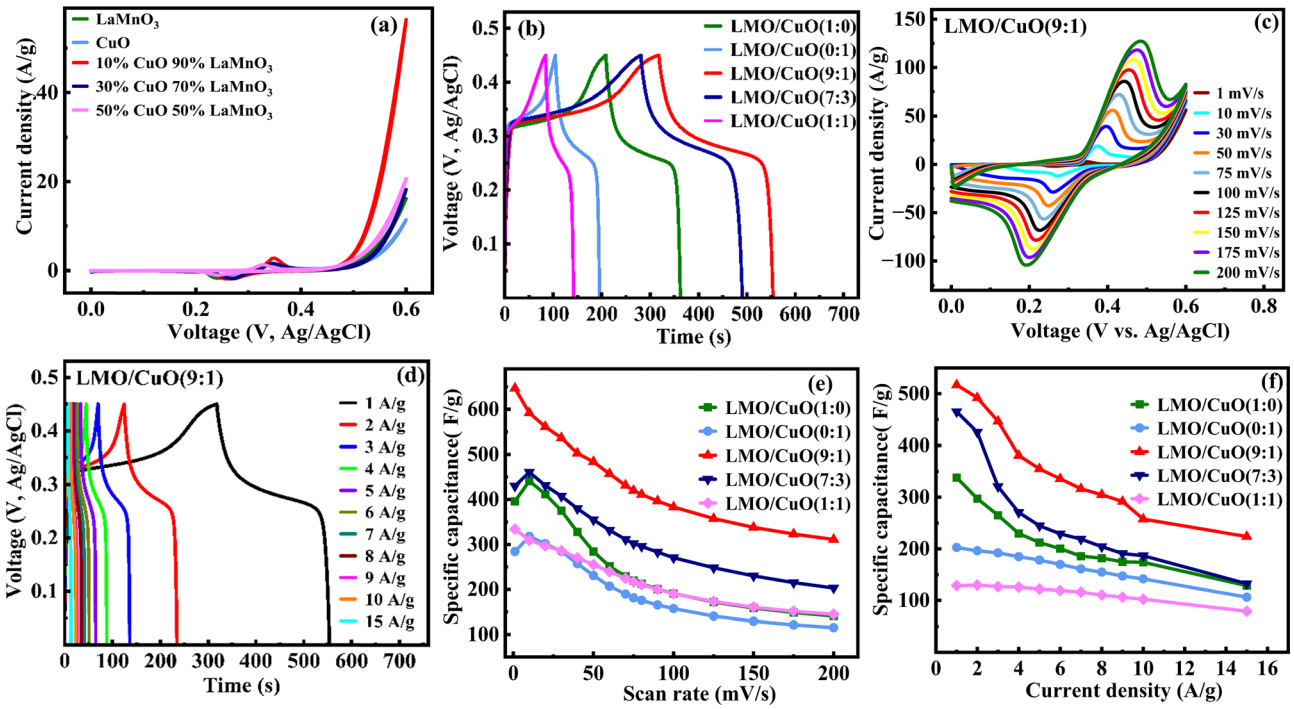

Fig. 5 (a) CV curves 1 mV s^{-1}, (b) chronopotentiometry charge/discharge (CCD) curves of s at 1 A g^{-1}. (c) CV curves as a function of scan rate, (d) GCDs of LMO/CuO(9 : 1) at different current densities, (e) C_{SP} *vs.* scan rates. (f) C_{SP} *vs.* current densities of LMO/CuO composites.

rate (v). For LMO/CuO(1 : 0), LMO/CuO(0 : 1), LMO/CuO(9 : 1), LMO/CuO(7 : 3), and LMO/CuO(1 : 1), the b-values are 0.59, 0.61, 0.63, 0.64, and 0.66, respectively. A more detailed picture is given in Fig. S2(a). The obtained b-values, ranging from 0.5 to 1.0, reflect a combined charge-storage mechanism involving both diffusion and surface (capacitively controlled) effects. To understand the diffusion coefficient of LMO/CuO composites, let us consider $b = 0.5$, then the power-law eqn (10) can be expressed in terms of the Randles–Sevcik equation (eqn (11)):[46]

$$i_p = 2.69 \times 10^5 AC_0(n^3 Dv/RT) \quad (11)$$

where i_p, A, C_0, n, D, R, T represent the peak current, surface area of the electrode material, surface concentration of the electrode, number of electrons involved in the reaction of the redox couple, diffusion coefficient, gas constant, and temperature, respectively. The relationship between peak current and the square root of the scan rate is a straight line, whose slope is proportional to the diffusion coefficient, as shown in Fig. S2(b). To understand the quantitative relationship between the diffusion-controlled and surface (capacitive)-controlled, Dunn's equation was used, as shown in eqn (12):[47]

$$i(V) = k_1 v + k_2 v^{1/2} \quad (12)$$

For analytical purposes, eqn (12) can be rearranged slightly to

$$\frac{i(V)}{v^{\frac{1}{2}}} = k_1 v^{\frac{1}{2}} + k_2 \quad (13)$$

In this equation, parameters k_1 and k_2 are constant. The current response for diffusion-controlled processes varies $v^{1/2}$, whereas for capacitive-controlled processes it varies directly with v. In detail, the relation between the $i(V)/v^{1/2}$ and $v^{1/2}$ gives a straight line with slope (k_1) and y-intercept (k_2) (eqn (13)). Solving for k_1 and k_2 at each potential allows us to qualitatively estimate the diffusion ($k_2 v^{1/2}$) and capacitive contributions ($k_1 v$). The diffusion percentage, even at 200 mV s^{-1}, is 76, 71, 64, 66, and 60% for LMO/CuO(1 : 0), LMO/CuO(0 : 1), LMO/CuO(9 : 1), LMO/CuO(7 : 3), and LMO/CuO(1 : 1), respectively, and shown in Fig. S2(c). The diffusion-controlled process that dominates the energy storage mechanism indicates a faradaic redox reaction.

The charge/discharge curves of LMO/CuO(9 : 1) at different current densities from 1 to 15 A g^{-1} are shown in Fig. 5(d). Distinct sloping plateau regions are observed across various current densities, consistent with typical pseudocapacitive behavior and consistent with the CV results. The CV profiles recorded at different scan rates and the corresponding charge–discharge curves measured at multiple current densities for LMO/CuO(1 : 0), LMO/CuO(0 : 1), LMO/CuO(7 : 3), and LMO/CuO(1 : 1) are shown in Fig. S3(a–h).

The C_{SP} was calculated from the CV curves by using eqn (2) and is 369, 284, 647, 430, and 334 F g^{-1} at 1 mV s^{-1} of LMO/CuO(1 : 0), LMO/CuO(0 : 1), LMO/CuO(9 : 1), LMO/CuO(7 : 3), and LMO/CuO(1 : 1), respectively, and shown in Fig. 5(e). The plot reveals that the C_{SP} decreases with increasing scan rate, which can be attributed to the electrochemical kinetics at the electrode–electrolyte interface. At lower scan rates, electrolyte ions have sufficient time to penetrate into the bulk of the electrode material, thereby increasing capacitance. In contrast, at higher scan rates, ion diffusion is limited, and ions primarily interact with the electrode surface, thereby reducing capacitance.

From the charge/discharge curves (eqn (3)), the C_{SP} at 1 A g^{-1} are 338, 203, 517, 465, and 129 F g^{-1}, as presented in Table S2. The calculation of the C_{SP} of LMO/CuO composites at different current densities is presented in Fig. 4(f). According to our previous work, the C_{SP} (10 F g^{-1} at 1 mV s^{-1}) from bare Ni-form could be ignored.[48] Table S2 presents the C_{SP} relationship with scan rate and current density for the LMO/CuO composites, including the E_d and P_d values. Here, the C_{SP} of LMO/CuO(9 : 1) composites is greater than others, maybe due to (i) the synergetic effect between the $LaMnO_3$ and CuO, and (ii) loose packing morphology. Further increasing the CuO ratio decreases the C_{SP}, likely due to particle agglomeration, thereby reducing the availability of redox-active sites.

Fig. 6(a) shows the electrochemical impedance spectroscopy (EIS) of LMO/CuO composites, with a well-fitted equivalent circuit that accounts for all impedance components. The frequency range is divided into three parts. In the low-frequency region, the slope of the curve corresponds to the Warburg impedance (W), which indicates electrolyte diffusion at the electrode.[49] In the low-frequency region, the Nyquist plot of LMO/CuO composites shows a straight line with a phase angle of approximately 70° (a vertical line for an ideal capacitor), indicating good capacitive behavior.[50] Such non-ideal behavior is typically represented in the equivalent circuit by incorporating a constant-phase element (CPE):[51]

$$Z_{CPE} = \frac{1}{Q(j\omega)^{\alpha}} \quad (14)$$

In eqn (14), Z_{CPE} represents the impedance of the constant phase element (CPE), j is the imaginary unit ($j^2 = -1$), and ω denotes the angular frequency defined as $\omega = 2\pi f$, where f is the frequency in Hertz (Hz). The parameters Q and α are frequency-independent constants, with Q. Corresponding to the interfacial differential capacitance. The dimensionless exponent α ($0 < \alpha \leq 1$) characterizes the deviation from ideal capacitive behavior. Z_{CPE} becomes a pure capacitor when $\alpha = 1$, a resistor when $\alpha = 0$, and a Warburg impedance when $\alpha = 0.5$. In the high-frequency region, the intersection of the Nyquist plot with the x-axis corresponds to the solution resistance (R_1), which includes the combined contributions from the intrinsic resistance of the substrate, the ionic resistance of the electrolyte, and the contact resistance at the interface between the active material and the current collector.[52] The small semicircle in the high frequency region indicates (inset Fig. 6(a)) the charge transfer resistance (R_2), which is the lowest value of 6.35 Ω for LMO/CuO(9 : 1). The fitted parameters obtained from the equivalent circuit model from Gamry Echem Analyst are summarized in Table S3. The lower R_2 value indicates faster charge-transfer kinetics at the electrode–electrolyte interface. The slope of the low-frequency region indicates the diffusion coefficient of the electrode materials.[49]

Long cyclic stability is the desired property of any efficient supercapacitor device. The cyclic stability test was performed by repeating the charge–discharge measurements of the LMO/CuO composites at 10 A g^{-1} in the same potential window (0–0.45 V) over 5000 cycles, as shown in Fig. 6(b) (solid symbols).

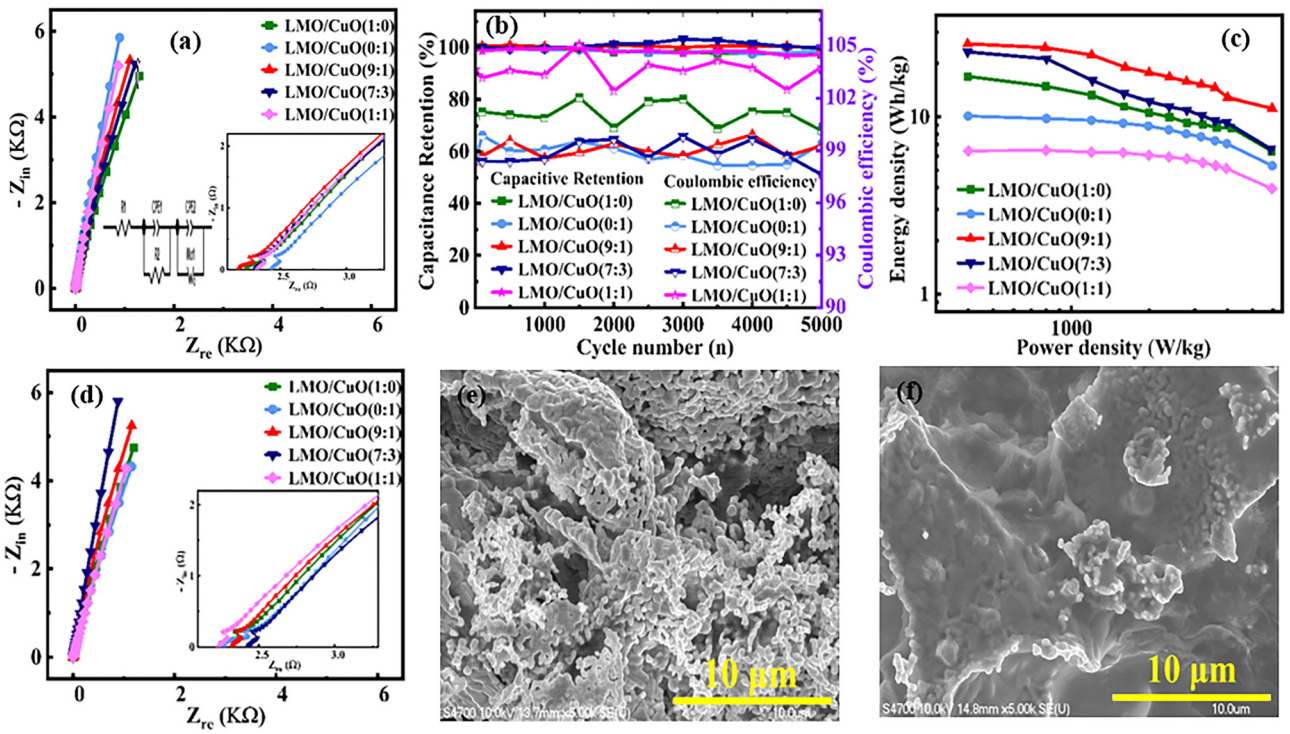

Fig. 6 (a) Nyquist plots with fitting equivalent circuit and high frequency region (inset), (b) long-term cyclic stability over 5000 charge–discharge cycles, showing capacitance retention (left axis) and Coulombic efficiency (right axis). (c) Relationship between log of E_d *vs.* P_d at different current densities from 1 to 15 A g^{-1} of LMO/CuO composites. (d) Nyquist plot after stability test, FESEM images of LMO/CuO(9 : 1) composites (e) before, and (f) after stability test.

We observed some capacitance fluctuations that may be attributed to temperature changes during continuous charging and discharging.[53] After 5000 cycles, the C_{SP} remains 175, 148, 234, 190, and 121 F g^{-1} for LMO/CuO(1 : 0), LMO/CuO(0 : 1), LMO/CuO(9 : 1), LMO/CuO(7 : 3), and LMO/CuO(1 : 1) with retention percentages of 97.2, 98.8, 99.8, 97.6, and 97.2%, respectively.

The Coulombic efficiency (η) was calculated by using the following eqn (15):[54]

$$\eta\% = \frac{t_d}{t_c} \times 100 \quad (15)$$

here, t_d and t_c are the discharging and charging times, respectively. Cyclic stability was measured at 10 A g^{-1} in a 1 M KOH solution. The coulombic efficiency remains above 97% for all composites, even at 5000 cycles (Fig. 6(b), half-filled symbols), demonstrating excellent cyclic stability in electrochemical capacitor applications. The Ragone plot illustrates the relationship between log(E_d) and log(P_d), where E_d and P_d are calculated using eqn (4) and (5), respectively, as shown in Fig. 6(c). LMO/CuO(9 : 1) composite has the highest E_d of 26 Wh kg^{-1} with respective P_d of 398 W kg^{-1}. Similarly, LMO/CuO(1 : 0), LMO/CuO(0 : 1), LMO/CuO(7 : 3), and LMO/CuO(1 : 1) have E_d of 17, 10, 23, and 6 Wh kg^{-1} with corresponding P_d of 399, 399, 398, and 401 W kg^{-1}, respectively, and presented in Table S2. The LMO/CuO composites exhibit respectable electrochemical performance in comparison with previously reported values, as summarized in Table S4. Fig. 6(d) represents the EIS measurements recorded after 5000 charge–discharge cycles (stability test). The R_2 values were found to be 9.65, 13.90, 7.25, 9.16, and 10.61 Ω for LMO/CuO(1 : 0), LMO/CuO(0 : 1), LMO/CuO(9 : 1), LMO/CuO(7 : 3), and LMO/CuO(1 : 1), respectively, listed in Table S5. R_2 values increased relative to those observed prior to cyclic stability, which can be attributed to partial electrode surface degradation and the formation of resistive layers during prolonged electrochemical cycling, as evidenced by FESEM images (Fig. 6(f)). Repeated ion intercalation/deintercalation and continuous exposure to the electrolyte may lead to structural distortion, surface passivation, and the accumulation of OH^- and K^+ ions at the active surface, thereby increasing charge-transfer and solution resistances. Fig. 6(e) presents the FESEM image of the LMO/CuO(9 : 1) electrode before the stability test, which closely resembles Fig. 2(c), indicating that the coating of the active material on the nickel foam is uniform and well-adhered. However, in the FESEM image (Fig. 6(f)), the particle surfaces of the LMO/CuO composites show reduced asperities after the 5000-cycle stability test, compared with their original morphology. This transformation can be attributed to several factors, including prolonged exposure to the alkaline electrolyte, which may lead to surface etching or the formation of passivation layers that can fill surface irregularities. The FESEM images of other composites before and after the stability test are presented in Fig. S4. The surfaces appear smoother after cyclic stability, although the overall morphology of the composites does not differ significantly from that of the source material.

In the $LaMnO_3$–CuO composite, the C_{SP} exhibits a pronounced enhancement at the 90 : 10 wt% ratio, attributable to an optimal synergistic interplay that maximizes heterogeneous interfaces and redox-active sites while mitigating agglomeration-induced drawbacks at higher CuO loadings. This composition fosters superior electronic conductivity, accelerated ion diffusion *via* oxygen vacancies, and balanced faradaic contributions from $LaMnO_3$'s anion intercalation and Mn^{3+}/Mn^{4+} redox processes, positioning it as the ideal "sweet spot" for pseudocapacitive performance. At the atomic level, CuO introduces $Cu^{2+} \leftrightarrow Cu^{1+}$ redox centers that complement Mn states through efficient d-orbital overlap, engineers lattice defects to enhance O^{2-} mobility and electrolyte adsorption, and tunes the electronic structure *via* p-type hole injection, thereby lowering charge-transfer barriers and boosting overall capacitance retention. The observed reduction in electrochemical performance at higher CuO content may arise from increased heterogeneity, which leads to CuO clusters and higher interparticle resistance within the composite. Additionally, these clusters block redox-active sites on the $LaMnO_3$ surface. Thus, at ~10% CuO, the composite achieves an optimal balance of Cu^{2+}/Cu^{1+} redox couples, and enhanced conductivity synergizes with Mn^{3+}/Mn^{4+} hopping without disrupting the perovskite framework.

Conclusion

$LaMnO_3$–CuO composites were synthesized *via* a facile auto-combustion route and thoroughly characterized to establish the correlation between their structure and electrochemical performance. Rietveld refinement confirmed the compositional ratios, while XRD verified the coexistence of distinct phases. XPS analysis revealed an increased concentration of oxygen vacancies, indicative of enhanced defect-assisted conductivity and redox activity. In contrast, BET measurements indicated a higher surface area for the LMO/CuO (9 : 1) composite, thereby facilitating efficient ion access. These structural and surface features collectively provide a favorable framework for charge storage. Electrochemical studies demonstrated that the LMO/CuO(9 : 1) composite achieved the best performance, delivering C_{SP} of 647 F g^{-1} at 1 mV s^{-1} and 517 F g^{-1} at 1 A g^{-1}, with excellent cyclic stability (99.8% retention after 5000 cycles). Overall, a 75% enhancement in specific capacitance is observed for LMO/CuO(9 : 1) compared to pure LMO. It also exhibited a high energy density of 26 Wh kg^{-1} at a power density of 398 W kg^{-1}. The superior performance is attributed to the synergistic interaction between $LaMnO_3$ and CuO, which enhances redox activity, electron transport, and defect chemistry. These results demonstrate that controlled incorporation of CuO (~10%) into $LaMnO_3$ provides an optimal balance of conductivity, stability, and capacitance, underscoring the potential of perovskite–oxide composites for next-generation supercapacitors.

Conflicts of interest

The authors declare that they have no known competing financial interests or personal relationships that could have appeared to influence the work reported in this paper.

Data availability

The data are available in following link: https://zenodo.org/uploads/17614003.

Supplementary information (SI) is available. See DOI: https://doi.org/10.1039/d5ya00339c.

Acknowledgements

NSF-CBET, Award #: 2434668. The authors would like to thank the Department of Physics and Materials Science and the Integrated Microscopic Center (IMC) at the University of Memphis for their support of this research.

References

1 P. Simon and Y. Gogotsi, Materials for electrochemical capacitors, *Nat. Mater.*, 2008, **7**, 845–854.
2 K. S. Kumar, N. Choudhary, Y. Jung and J. Thomas, Recent advances in two-dimensional nanomaterials for supercapacitor electrode applications, *ACS Energy Lett.*, 2018, **3**, 482–495.
3 A. W. Anwar, A. Majeed, N. Iqbal, W. Ullah, A. Shuaib and U. Ilyas, *et al.*, Specific capacitance and cyclic stability of graphene based metal/metal oxide nanocomposites: a review, *J. Mater. Sci. Technol.*, 2015, **31**(7), 699–707.
4 Q. Wei, F. Xiong, S. Tan, L. Huang, E. H. Lan and B. Dunn, *et al.*, Porous one-dimensional nanomaterials: design, fabrication and applications in electrochemical energy storage, *Adv. Mater.*, 2017, **29**, 1602300.
5 P. Ma, N. Lei, B. Yu, Y. Liu, G. Jiang and J. Dai, *et al.*, Flexible supercapacitor electrodes based on carbon cloth-supported LaMnO3/MnO nano-arrays by one-step electrodeposition, *Nanomaterials*, 2019, **9**, 1676.
6 Z. Yu, B. Duong, D. Abbitt and J. Thomas, Highly ordered MnO2 nanopillars for enhanced supercapacitor performance, *Adv. Mater.*, 2013, **25**, 3302–3306.
7 B. Song, C. Sizemore, L. Li, X. Huang, Z. Lin and K. S. Moon, *et al.*, Triethanolamine functionalized graphene-based composites for high performance supercapacitors, *J. Mater. Chem. A*, 2013, **3**, 21789–21796.
8 J. Tripathi, V. Salve, Z. Ansari, S. Patange, P. Thakur and V. Chavan, *et al.*, Tailored MIL-101, *Ionics*, 2025, 907–922.
9 G. Kothandam, G. Singh, X. Guan, J. M. Lee, K. Ramadass and S. Joseph, *et al.*, Recent advances in carbon-based electrodes for energy storage and conversion, *Adv. Sci.*, 2023, **10**, 2301045.
10 R. R. Salunkhe, Y. V. Kaneti and Y. Yamauchi, Metal–organic framework-derived nanoporous metal oxides toward supercapacitor applications: progress and prospects, *ACS Nano*, 2017, **11**, 5293–5308.
11 C. D. Lokhande, D. P. Dubal and O. S. Joo, Metal oxide thin film based supercapacitors, *Curr. Appl. Phys.*, 2011, **11**, 255–270.
12 C. C. Hu and W. C. Chen, Effects of substrates on the capacitive performance of RuOx nH2O and activated carbon–RuOx electrodes for supercapacitors, *Electrochim. Acta*, 2004, **49**, 3469–3477.
13 J. T. Mefford, W. G. Hardin, S. Dai, K. P. Johnston and K. J. Stevenson, Anion charge storage through oxygen intercalation in LaMnO3 perovskite pseudocapacitor electrodes, *Nat. Mater.*, 2014, **13**, 726–732.
14 X. Xu, S. Li, H. Zhang, Y. Shen, S. M. Zakeeruddin and M. Graetzel, *et al.*, A power pack based on organometallic perovskite solar cell and supercapacitor, *ACS Nano*, 2015, **9**, 1782–1787.
15 P. Gao, M. Grätzel and M. K. Nazeeruddin, Organohalide lead perovskites for photovoltaic applications, *Energy Environ. Sci.*, 2014, **7**, 2448–2463.
16 P. M. Shafi, N. Joseph, A. Thirumurugan and A. C. Bose, Enhanced electrochemical performances of agglomeration-free LaMnO3 perovskite nanoparticles and achieving high energy and power densities with symmetric supercapacitor design, *Chem. Eng. J.*, 2018, **338**, 147–156.
17 V. Senthilkumar, Y. S. Kim, S. Chandrasekaran, B. Rajagopalan, E. J. Kim and J. S. Chung, Comparative supercapacitance performance of CuO nanostructures for energy storage device applications, *RSC Adv.*, 2015, **5**, 20545–20553.
18 A. Arya, S. Tanwar, M. Iqbal, A. Sharma and A. L. Sharma, Synergetic effect driven LaMnO3@ NiO composite based high energy semi-solid supercapacitor, *J Energy Storage*, 2025, **105**, 114778.
19 A. Dhakal, F. A. Perez, S. Karna and S. R. Mishra, LaMnO3-Mn3O4 nanocomposite: Synergetic effect towards high electrochemical performance, *J. Alloys Compd.*, 2024, **1008**, 176262.
20 P. M. Shafi, V. Ganesh and A. C. Bose, LaMnO3/RGO/PANI ternary nanocomposites for supercapacitor electrode application and their outstanding performance in all-solid-state asymmetrical device design, *ACS Appl. Energy Mater.*, 2018, **1**, 2802–2812.
21 B. Patil, R. Jagtap, D. Narkhede and S. Pardeshi, Design of LaMnO3/rGO composite electrode materials for high-performance energy storage devices. Discover, *Electrochemistry*, 2025, **2**, 1.
22 S. Nagamuthu, S. Vijayakumar and K. S. Ryu, Cerium oxide mixed LaMnO3 nanoparticles as the negative electrode for aqueous asymmetric supercapacitor devices, *Mater. Chem. Phys.*, 2017, **199**, 543–551.
23 R. Packiaraj, K. Mahendraprabhu, P. Devendran, N. Nallamuthu, B. Palanivel and K. S. Venkatesh, *et al.*, Electrochemical performances of ZnO–NiO–CuO mixed metal oxides as smart electrode material for solid-state asymmetric device fabrication, *Energy Fuels*, 2021, **361**, 603–617.
24 K. M. Racik, A. Manikandan, M. Mahendiran, P. Prabakaran, J. Madhavan and M. V. A. Raj, Fabrication of manganese oxide decorated copper oxide (MnO2/CuO) nanocomposite electrodes for energy storage supercapacitor devices, *Phys. E*, 2020, **119**, 114033.
25 J. Gazquez, S. Bose, M. Sharma, M. A. Torija, S. J. Pennycook and C. Leighton, *et al.*, Lattice mismatch accommodation via oxygen vacancy ordering in epitaxial $La_{0.5}Sr_{0.5}CoO_{3-\delta}$ thin films, *APL Mater.*, 2013, **1**(1), 012105.

26 A. Dhakal, F. A. Perez and S. R. Mishra, Electrochemical assessment of tailored Mn_2O_3 cuboidal hierarchical particles prepared using urea and Piperazine, *Electrochim. Acta*, 2024, **507**, 145169.
27 M. Sethi, U. S. Shenoy and D. K. Bhat, A porous graphene–NiFe2O4 nanocomposite with high electrochemical performance and high cycling stability for energy storage applications, *Nanoscale Adv.*, 2020, **2**, 4229–4241.
28 Y. Wang, Y. Song and Y. Xia, Electrochemical capacitors: mechanism, materials, systems, characterization and applications, *Chem. Soc. Rev.*, 2016, **45**, 5925–5950.
29 J. Yan, T. Wei, B. Shao, Z. Fan, W. Qian and M. Zhang, *et al.*, Preparation of a graphene nanosheet/polyaniline composite with high specific capacitance, *Carbon*, 2010, **48**, 487–493.
30 A. J. Bard, L. R. Faulkner and H. S. White, *Electrochemical methods: fundamentals and applications*, John Wiley and Sons, 2022.
31 U. Vladimir and I. Popov, Metrological characterization of X-ray diffraction methods for determination of crystallite size in nano-scale materials, *Mater. Charact.*, 2013, **58**, 883–891.
32 V. Salve, P. Agale, S. Balgude, S. Mardikar, S. Dhotre and P. More, Enhanced photocatalytic activity of SnO2@ gC3N4 heterojunctions for methylene blue and bisphenol-A degradation: effect of interface structure and porous nature, *RSC Adv.*, 2025, **15**, 15651–15669.
33 M. Thommes, K. Kaneko, A. V. Neimark, J. P. Olivier, F. Rodriguez-Reinoso, J. Rouquerol, *et al.*, *Physisorption of gases*, 2015.
34 A. Dhakal, F. Perez and S. R. Mishra, Unveiling the Synergistic Potential of LaMnO3-CeO2 Composites in Supercapacitor Applications, *RSC Sustainability*, 2025, **3**, 5556–5570.
35 P. P. Ma, Q. L. Lu, N. Lei, Y. K. Liu, B. Yu and J. M. Dai, *et al.*, Effect of A-site substitution by Ca or Sr on the structure and electrochemical performance of LaMnO3 perovskite, *Electrochim. Acta*, 2020, **332**, 135489.
36 H. Mo, H. Nan, X. Lang, S. Liu, L. Qiao and X. Hu, *et al.*, Influence of calcium doping on performance of LaMnO3 supercapacitors, *Ceram. Int.*, 2018, **44**, 9733–9741.
37 H. W. Nesbitt and D. J. A. M. Banerjee, Interpretation of XPS Mn (2p) spectra of Mn oxyhydroxides and constraints on the mechanism of MnO2 precipitation, *Am. Mineral.*, 1998, **83**, 305–315.
38 J. Balamurugan, C. Li, T. D. Thanh, O. K. Park, N. H. Kim and J. H. Lee, Hierarchical design of $Cu_{1-x}Ni_xS$ nanosheets for high-performance asymmetric solid-state supercapacitors, *J. Mater. Chem. A*, 2017, **5**, 19760–19772.
39 Z. Luo, R. Miao, T. D. Huan, I. M. Mosa, A. S. Poyraz and W. Zhong, *et al.*, Mesoporous MoO_{3-x} material as an efficient electrocatalyst for hydrogen evolution reactions, *Adv. Energy Mater.*, 2016, **6**, 1600528.
40 X. Lu, Y. Zeng, M. Yu, T. Zhai, C. Liang and S. Xie, *et al.*, Oxygen-deficient hematite nanorods as high-performance and novel negative electrodes for flexible asymmetric supercapacitors, *Adv. Mater.*, 2014, **26**, 3148–3155.
41 M. Kandasamy, S. Sahoo, S. K. Nayak, B. Chakraborty and C. S. Rout, Recent advances in engineered metal oxide nanostructures for supercapacitor applications: experimental and theoretical aspects, *J. Mater. Chem. A*, 2021, **9**, 17643–17700.
42 H. Zhao, Q. Zhu, X. Ye, L. Wang and S. Dong, Electrochemical properties of LaMO3 (M= Cr, Mn, and Co) perovskite materials, *Coatings*, 2024, **14**, 147.
43 X. Ye, S. Dong, X. Jin, J. Wei, L. Wang and Y. Zhang, Enhancement in the electrochemical performance of strontium (Sr)-doped LaMnO3 as supercapacitor materials, *Coatings*, 2022, **12**, 1739.
44 A. Ajith, E. Thomas, C. H. Suresh and R. R. Philip, Advances and strategies in nanoarchitectured TiO2-based electrodes for supercapacitors, *J. Energy Storage*, 2025, **111**, 115289.
45 H. Lindström, S. Södergren, A. Solbrand, H. Rensmo, J. Hjelm and A. Hagfeldt, *et al.*, Li+ ion insertion in TiO2 (anatase). 2. Voltammetry on nanoporous films, *J. Phys. Chem. B*, 1997, **101**, 7717–7722.
46 J. E. Randles, A cathode ray polarograph. Part II. The current-voltage curves, *Trans. Faraday Soc.*, 1948, **44**, 327–338.
47 T. C. Liu, W. G. Pell, B. E. Conway and S. L. Roberson, Behavior of molybdenum nitrides as materials for electrochemical capacitors: comparison with ruthenium oxide, *J. Electrochem. Soc.*, 1998, **145**, 1882.
48 A. Dhakal, S. R. Mishra and F. Perez, Urea-Driven Hydrothermal Synthesis of Mn2O3: Electrochemical Performance Across Various Electrolytes for Supercapacitor Applications, *Energy Adv.*, 2025, **4**, 878–895.
49 C. Guan, J. Liu, C. Cheng, H. Li, X. Li and W. Zhou, *et al.*, Hybrid structure of cobalt monoxide nanowire@ nickel hydroxidenitrate nanoflake aligned on nickel foam for high-rate supercapacitor, *Energy Environ. Sci.*, 2011, **4**, 4496–4499.
50 Y. Gao, S. Chen, D. Cao, G. Wang and J. Yin, Electrochemical capacitance of Co3O4 nanowire arrays supported on nickel foam, *J. Power Sources*, 2010, **195**, 1757–1760.
51 J. Wang, J. Polleux, J. Lim and B. Dunn, Pseudocapacitive contributions to electrochemical energy storage in TiO2 (anatase) nanoparticles, *J. Phys. Chem. C*, 2007, **111**, 14925–14931.
52 C. Peng, L. Yanyue, J. Yuanyuan, W. Haiyan and L. Zijiong, Synthesis of LaMnO3-reduced graphene oxide or Sr composite and their application in electrochemical properties, *Mater. Res. Express*, 2020, **7**, 25023.
53 H. M. El Sharkawy, A. S. Dhmees, A. R. Tamman, S. M. El Sabagh, R. M. Aboushahba and N. K. Allam, N-doped carbon quantum dots boost the electrochemical supercapacitive performance and cyclic stability of MoS2, *J. Energy Storage*, 2020, **27**, 101078.
54 A. Noori, M. F. El-Kady, M. S. Rahmanifar, R. B. Kaner and M. F. Mousavi, Towards establishing standard performance metrics for batteries, supercapacitors and beyond, *Chem. Soc. Rev.*, 2019, **48**, 1272–1341.